Journal of
Materials Chemistry A

ROYAL SOCIETY
OF CHEMISTRY

PAPER

View Article Online
View Journal | View Issue

Check for updates

Cite this: *J. Mater. Chem. A*, 2023, **11**, 10328

Atomically dispersed ruthenium sites with electron-rich environments in intermetallic compounds for high-current-density hydrogen evolution†

Huaifang Zhang,‡[ab] Chuanqi Cheng,‡[c] Jin Zhou,‡[d] Chaoqun Ma,[ab] Peidong Shi,[e] Haoming Wu,[ab] Pengfei Yin,[c] Wenbin Cao,[a] Jing Xia,[f] Lijie Zhu,*[g] An-Liang Wang*[e] and Qipeng Lu*[abh]

Industrial electrocatalytic hydrogen production puts forward high requirements for catalysts. Compared to the traditional disordered alloy electrocatalysts, intermetallic compounds (IMCs) with ordered atomic arrangement exhibit higher mixing enthalpy and stronger atomic interactions, which greatly improves their catalytic performance and structural stability. Herein, we rationally design and precisely prepare ordered RuGa IMCs with the body-centered cubic structure on N-doped reduced graphene oxide supports (RuGa/N-rGO), which exhibit remarkable HER activities in both acidic and alkaline electrolytes. Notably, the obtained electrocatalyst requires extremely low overpotentials of 105 and 156 mV to deliver 500 and 1000 mA cm^{-2}, respectively, along with high stability over 100 hours continuously running at the overpotential of 100 mV in alkaline electrolyte. Experimental characterizations and theoretical simulations indicate that the Ru sites with electron-rich environments are isolated in RuGa/N-rGO, which significantly reduces the energy barrier of the rate-limiting step during the HER process. This work provides valuable insights into the atomic modulation of active sites for enhanced catalytic performance, paving a way for designing advanced noble metal-based electrocatalysts.

Received 6th March 2023
Accepted 26th April 2023

DOI: 10.1039/d3ta01376f

rsc.li/materials-a

---

[a] *School of Materials Science and Engineering, University of Science and Technology Beijing, Beijing 100083, China. E-mail: qipeng@ustb.edu.cn*

[b] *Shunde Innovation School, University of Science and Technology Beijing, Foshan 528399, China*

[c] *Institute of New Energy Materials, School of Materials Science and Engineering, Tianjin University, Tianjin 300072, China*

[d] *School of Chemical Engineering and Technology, Tianjin University, Tianjin 300072, China*

[e] *School of Chemistry and Chemical Engineering, Shandong University, Jinan 250100, China. E-mail: alwang@sdu.edu.cn*

[f] *Key Laboratory of Photochemical Conversion and Optoelectronic Materials, Technical Institute of Physics and Chemistry, Chinese Academy of Sciences, Beijing 100190, China*

[g] *School of Instrument Science and Opto-Electronics Engineering, Beijing Information Science and Technology University, Beijing 100192, China. E-mail: ljzhu@bistu.edu.cn*

[h] *Zhongguancun Institute of Human Settlements Engineering and Materials, Beijing 100083, China*

† Electronic supplementary information (ESI) available. See DOI: https://doi.org/10.1039/d3ta01376f

‡ These authors contributed equally to this work.

Qipeng Lu received his B.E. degree from the Taiyuan University of Technology in 2008. He obtained his M.E. and PhD degrees from Beijing Jiaotong University in 2010 and 2014, respectively. As a visiting student, he studied in Prof. Yadong Yin's group at the University of California, Riverside, from 2011 to 2013. He then carried out his postdoctoral research with Prof. Hua Zhang at Nanyang Technological University, Singapore, in 2014. In 2018, he joined the faculty of the School of Materials Science and Engineering, University of Science and Technology Beijing. His research interests are related to the synthesis of nanostructured metallic materials for energy conversion and catalysis.

Introduction

The severe environmental pollution and urgent energy demands have led to the exploration of renewable and green energy sources.[1–3] Hydrogen (H_2) is identified as a clean energy source to replace conventional fossil fuels because of its high energy density and zero carbon emissions.[4–6] The electrocatalytic hydrogen evolution reaction (HER) is an efficient and promising technology for eco-friendly and large-scale H_2 production driven by sustainable energy.[7–9] However, industrial HER electrocatalysts have to withstand harsh working conditions, including large current densities, strong alkaline/acidic electrolytes, and high temperatures,[10–12] which pose great challenges to the long-term usage of electrocatalysts. To date, platinum (Pt)-based nanomaterials with near-zero onset overpotential and extremely low Tafel slope are the most efficient HER electrocatalysts.[13–15] Unfortunately, Pt is scarce, and Pt-based alloys as electrocatalysts lack stability when operating at large current densities.[16,17] Thus, the rational design of high-performance and cost-effective electrocatalysts for industrial HER becomes highly necessary.

Ruthenium (Ru)-based electrocatalysts are expected to be ideal candidates to achieve the optimal HER performance because of their Pt-like metal–H bond strength and relatively low price.[18–21] To enhance the HER performance and decrease the consumption of Ru, the fabrication of composition-defined and atomic ordered Ru-based intermetallic compounds (IMCs) is a promising strategy.[22–26] The insertion of a relatively lower electronegative metal (*i.e.*, Ga) could create electron-rich environments for the Ru atoms,[27–30] which can modulate the electronic structure of Ru sites and improve the HER performance. In addition, the higher mixing enthalpy and stronger interactions between Ru and Ga atoms can firmly stabilize Ru atoms during the electrochemical measurements in both acidic and alkaline electrolytes.[31–33] Therefore, the development of Ru-based IMCs with high activity and stability is significant for industrial hydrogen production.

In this work, we successfully prepare ordered RuGa IMCs with the body-centered cubic (*bcc*) phase supported on N-doped reduced graphene oxide (RuGa/N-rGO) as a superior and stable HER electrocatalyst. As demonstrated by atomic resolution scanning transmission electron microscopy (STEM) images, Ru and Ga atoms are orderly arranged. The as-synthesized electrocatalyst exhibits outstanding HER performance with extremely low overpotentials of 32 mV (acidic electrolyte) and 20 mV (alkaline electrolyte) at 10 mA cm^{-2}, surpassing those of mostly reported Ru-based electrocatalysts. In addition, this electrocatalyst also possesses remarkable HER performance at large current densities in alkaline condition, achieving overpotentials of 105 and 156 mV at 500 and 1000 mA cm^{-2}, respectively, together with impressive stability (more than 100 hours continuously working at the overpotential of 100 mV). Theoretical simulations reveal that the Ga atoms could provide electron-rich environments for the body-centered Ru atoms, thereby decreasing the energy barrier of the rate-limiting step and boosting HER performance.

Results and discussion

The RuGa/N-rGO catalyst is synthesized through a modified impregnation-reduction method (see Experimental section for more details). By simplifying the complicated preparation process, the scale-up synthesis of RuGa/N-rGO (∼1.0 g) can be realized (Fig. S1†). As revealed by the high-angle annular dark-field scanning transmission electron microscopy (HAADF-STEM) image (Fig. 1a), the RuGa nanoparticles (RuGa NPs) with an average diameter of 5.5 ± 0.8 nm are uniformly anchored on the N-rGO substrates. The X-ray diffraction (XRD) pattern of RuGa/N-rGO (Fig. 1b) presents a typical *bcc* RuGa structure ($Pm\bar{3}m$, JCPDS No. 65-9178), and a weak peak appearing at 26.3° can be assigned to the graphitized carbon substrates. As shown in Fig. S2,† Ru/N-rGO fabricated with the similar procedure (see Experimental section for more details) matches with the hexagonal close-packed structure (JCPDS No. 06-0663). The inset of Fig. 1b illustrates the crystal structure of *bcc* RuGa phase with Ga atoms at eight corners and Ru atom occupying the body center. The scanning electron microscopy (SEM) image of RuGa/N-rGO (Fig. S3†) reveals a three-dimensional (3D) porous network consisting of cross-linked N-rGO nanosheets. Based on the N_2 adsorption–desorption results (Fig. S4†), the RuGa/N-rGO sample possesses a large specific surface area of 118.74 $m^2\ g^{-1}$, which ensures that abundant active sites can be exposed.[34,35] According to the atomic force microscopy (AFM) images (Fig. S5 and S6†), the thicknesses of RuGa/N-rGO and Ru/N-rGO are estimated to be approximately 7.0 nm. Moreover, based on the HAADF-STEM image (Fig. 1a) and TEM image (Fig. S7†), the RuGa NPs (∼5.5 nm) and Ru NPs (∼5.8 nm) are uniformly anchored on the N-rGO substrates. As the single-layer graphene has a theoretical thickness of 0.335 nm, it can be estimated that 4–5 layers of graphene exist in both RuGa/N-rGO and Ru/N-rGO. The ordered atomic arrangement of RuGa/N-rGO can be directly characterized by the aberration-corrected HAADF-STEM. Since the HAADF-STEM image reflects the atomic number (*Z*)-contrast of elements, the brightness of Ru atoms is relatively higher compared to that of Ga atoms. The aberration-corrected HAADF-STEM image of one RuGa particle reveals a typical ordered *bcc* phase through the direction of [001] zone axis (Fig. 1c), where Ru atoms are adjacent to four Ga atoms in a periodic square arrangement. The measured lattice distance of 2.13 Å is indexed to the *bcc* RuGa (110) plane. From the magnified yellow area in Fig. 1c, the highly ordered arrangement of Ru and Ga atoms matches well with the simulated structure model of *bcc* RuGa IMCs (Fig. 1d and e). Moreover, the fast Fourier transforms (FFT) pattern (Fig. 1f) proves the *bcc* structure, which agrees well with the simulated diffractogram pattern of *bcc* RuGa IMCs (Fig. 1g). To investigate the elemental distribution of RuGa particle, energy-dispersive X-ray spectroscopy (EDX) elemental mappings are acquired. As displayed in Fig. 1h, Ru and Ga elements are homogeneously distributed throughout the entire particle. The determined Ru/Ga atomic ratio is 51.1 : 48.9 based on the EDX analysis (Fig. S8†), which is close to the results from the

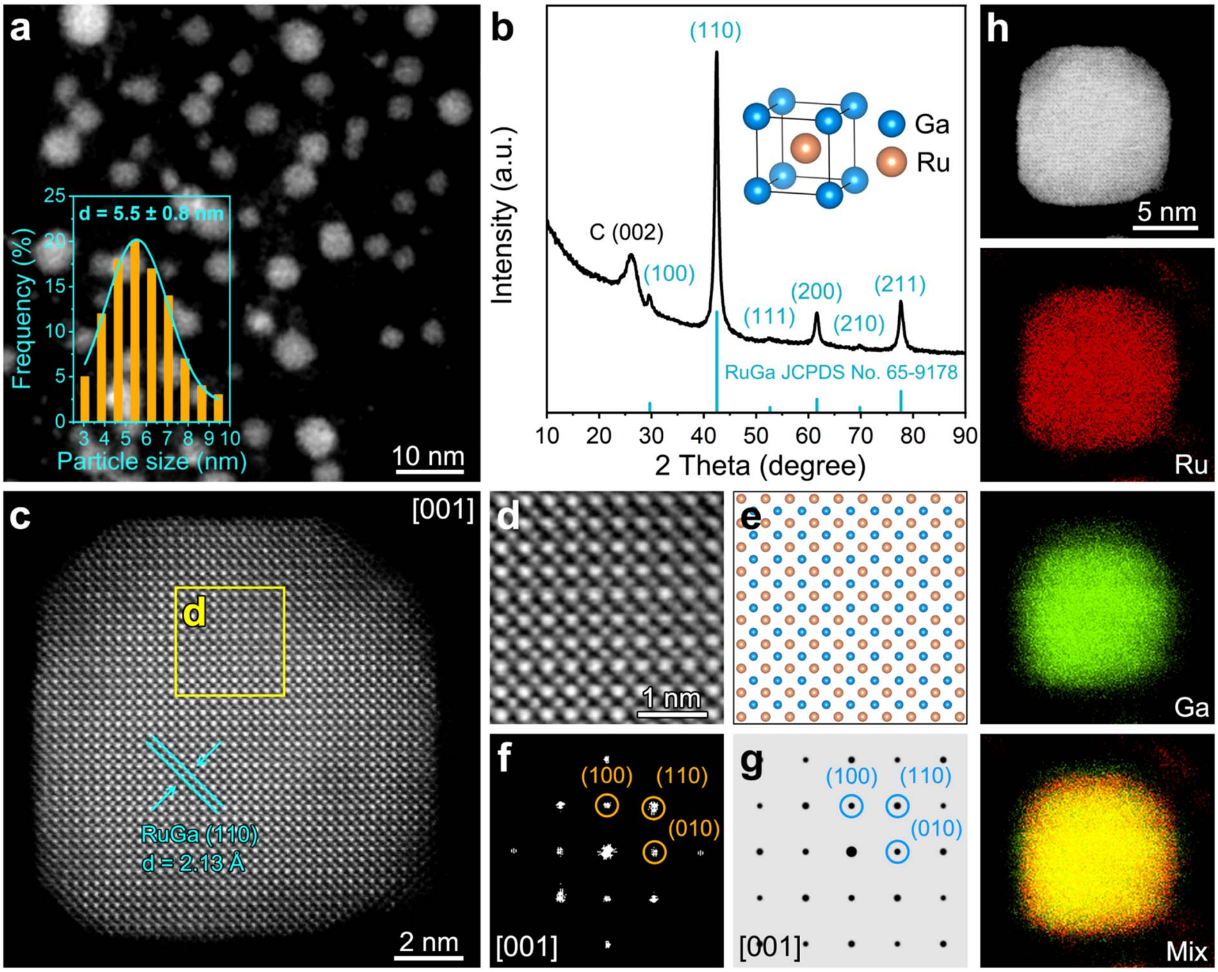

Fig. 1 Morphological and structural characterizations. (a) HAADF-STEM image of RuGa/N-rGO and the distribution histogram of particle diameter (inset). (b) XRD pattern of RuGa/N-rGO, the inset presents the crystal structure of *bcc* RuGa phase. (c) Typical atomic-resolution HAADF-STEM image of one RuGa particle through the direction of the [001] zone axis. (d) The magnified yellow area in (c) and (e) simulated structure model of *bcc* RuGa IMCs viewed from the [001] zone axis direction. The orange and blue spheres refer to Ru and Ga atoms, respectively. (f) The FFT pattern and (g) simulated diffractogram pattern of *bcc* RuGa IMCs oriented in the [001] zone axis. (h) HAADF-STEM-EDS elemental mappings of RuGa/N-rGO.

inductively coupled plasma atomic emission spectroscopy (ICP-AES) (Table S1†).

X-ray photoelectron spectroscopy (XPS) spectra are adopted for the surface analysis of materials. The XPS survey spectrum (Fig. 2a) indicates that the RuGa/N-rGO consists of C, N, Ru, Ga, and O elements. The existence of N (~6.2 at%) is derived from the pyrolysis of nitrate precursors during the thermal annealing process. The Ru 3p and Ga 3d XPS spectra (Fig. 2b and c) reveal that the mostly metallic state of Ru and the partially oxidized state of Ga (Ga^{n+}, $0 < n < 3$) coexist in RuGa/N-rGO. The negative shift of Ru 3p peak (~0.2 eV) is clearly observed in RuGa/N-rGO relative to that of Ru/N-rGO, which is caused by the electron donation from Ga to Ru atoms.[36,37] As presented in Fig. 2d, the C–N peak positioned at 285.9 eV proves the successful incorporation of N element into the rGO nanosheets. From the N 1s spectrum (Fig. 2e), the deconvoluted peaks located at 396.6, 398.4, and 400.9 eV are ascribed to the N–Ga, pyridinic-N, and graphitic-N, respectively. The graphitization degree of the carbon materials is evaluated by Raman spectroscopy (Fig. 2f). Two peaks located at 1350 and 1590 cm^{-1} are attributed to the D-band (defects and disordered carbon) and G-band (sp^2-hybridized carbon), respectively. The intensity ratios between D-band and G-band (I_D/I_G) of RuGa/N-rGO, Ru/N-rGO, and N-rGO are determined to be 1.36, 1.12, 0.96, respectively, higher than that of rGO (0.90), which is owing to the defects introduced by N doping and the deposition of metal NPs.[38,39]

It has been demonstrated that high annealing temperature is the driving force to form the ordered intermetallic phases.[40,41] Fig. S9† shows the XRD patterns of RuGa/N-rGO obtained at 500, 700, 800, and 900 °C with the reaction time of 12 hours, respectively. For annealed samples at 500 °C, the RuGa exhibits low crystallinity. As the temperature rises to 700 °C, the (100) superlattice peak begins to appear, which demonstrates that the intermetallic phase is forming. With further increasing temperature, the characteristic diffraction peaks become stronger and narrower, indicating that the increased annealing

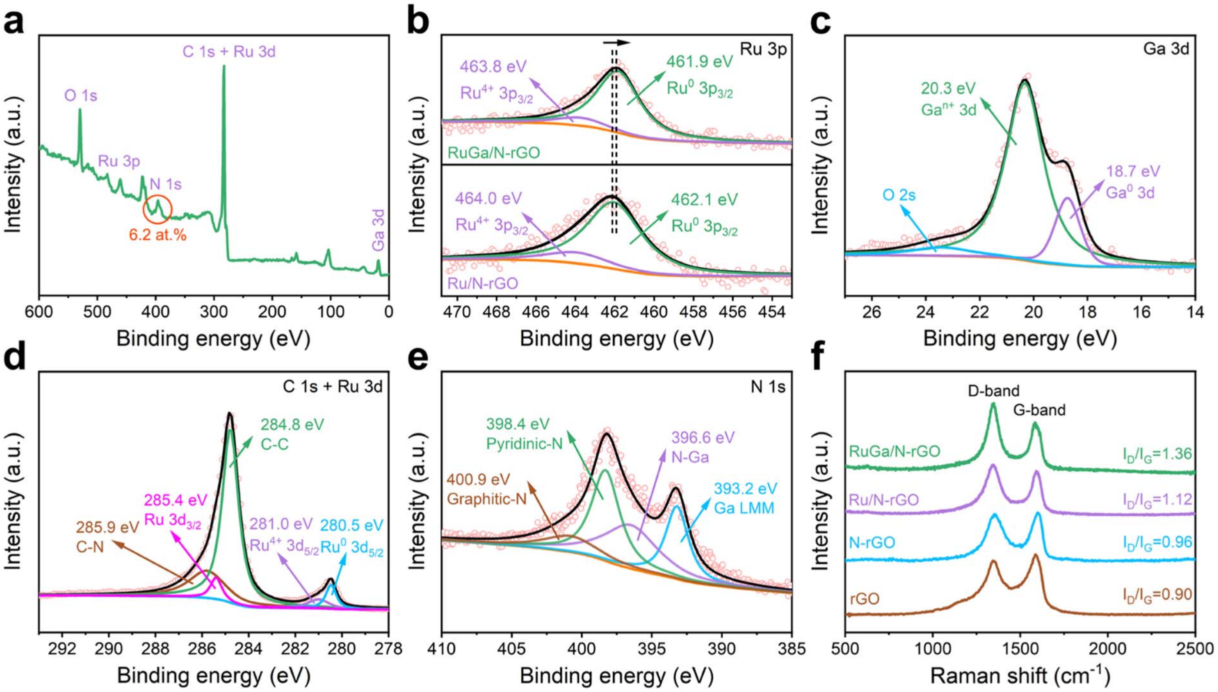

Fig. 2 (a) XPS survey spectrum of RuGa/N-rGO. (b) Ru 3p XPS spectra of Ru/N-rGO and RuGa/N-rGO. (c) Ga 3d, (d) C 1s + Ru 3d, and (e) N 1s XPS spectra of RuGa/N-rGO. (f) Raman spectra of rGO, N-rGO, Ru/N-rGO, and RuGa/N-rGO.

temperature leads to improved crystallinity and larger particle size. Specifically, the average diameters of RuGa NPs increase from 4.1 ± 0.4 to 8.5 ± 2.1 nm (Fig. S10 and S11†). Herein, the RuGa/N-rGO obtained at 700, 800, and 900 °C for 12 hours are designated as RuGa/N-rGO-*n* ($n = 1, 2, 3$), respectively.

The acidic HER activities of the as-prepared RuGa/N-rGO-*n* ($n = 1, 2, 3$) are first evaluated in N_2-purged 0.5 M H_2SO_4 electrolyte using a typical three-electrode system. For comparison, pure N-rGO, Ru/N-rGO, and commercial Pt/C are also evaluated under the identical working conditions. All the potential values presented in this paper are converted to the reversible hydrogen electrode (RHE). Fig. 3a shows the linear sweep voltammetry (LSV) polarization curves of each sample. It is noticeable that the electrocatalytic activity can be optimized by controlling the particle size and crystallinity degree of *bcc* RuGa.[42,43] As expected, RuGa/N-rGO-2 displays the most superior HER performance among all RuGa/N-rGO catalysts, while pure N-rGO exhibits negligible activity. Specifically, the overpotential value of RuGa/N-rGO-2 (32 mV) at 10 mA cm^{-2} is similar to that of commercial Pt/C (35 mV) and remarkably lower than those of RuGa/N-rGO-1 (43 mV), RuGa/N-rGO-3 (54 mV), and Ru/N-rGO (92 mV) (Fig. 3b). The Tafel plots are usually employed to explore reaction kinetics and mechanisms, and a smaller value of Tafel slope represents faster HER kinetics. RuGa/N-rGO-2 has a relatively low Tafel slope value of 29.0 mV dec^{-1} (Fig. 3c), which is smaller than those of commercial Pt/C (31.2 mV dec^{-1}), RuGa/N-rGO-1 (36.9 mV dec^{-1}), RuGa/N-rGO-3 (48.2 mV dec^{-1}), and Ru/N-rGO (80.9 mV dec^{-1}), suggesting the accelerated HER kinetics. Meanwhile, the low value of Tafel slope means that the HER process over RuGa/N-rGO-2 follows the Volmer–Tafel pathway.[44] Remarkably, the HER activities over RuGa/N-rGO-2 in 0.5 M H_2SO_4 solution surpass those of most recently published Ru-based electrocatalysts (Table S2†). The electrochemically active surface area (ECSA) of the electrocatalyst is well linearly related to the value of double-layer capacitance (C_{dl}) calculated from the cyclic voltammogram (CV) curves at various scan rates between 0.1 and 0.2 V (non-faradic potential range) (Fig. S12†). The calculated C_{dl} value of RuGa/N-rGO-2 is 24.64 mF cm^{-2} (Fig. 3d), which is much higher than those of RuGa/N-rGO-1 (16.47 mF cm^{-2}), RuGa/N-rGO-3 (11.72 mF cm^{-2}), and Ru/N-rGO (5.67 mF cm^{-2}), attributed to the interconnected 3D porous structure exposing abundant active sites. In addition, electrochemical impedance spectroscopy (EIS) experiments are conducted to study the electron/proton transfer during the HER process. As shown in the Nyquist plots (Fig. 3e), the smallest charge transfer resistance (R_{ct}) value of RuGa/N-rGO-2 is beneficial for the electron/proton transfer. The electrochemical stability of RuGa/N-rGO-2 is further assessed by the accelerated degradation tests and chronoamperometric measurement. As observed from Fig. 3f, the LSV polarization curves before and after 10 000 cycles keep nearly unchanged. In addition, the chronoamperometric curve indicates no significant degradation of current density for 26 hours at the constant overpotential of 30 mV (inset of Fig. 3f). After the long-term durability test, RuGa/N-rGO-2 exhibits remarkable structural stability without obvious particle size, crystal structure, and morphology changes (Fig. S13 and S14†).

The excellent HER properties of RuGa/N-rGO-2 are also evaluated under alkaline media. Fig. 4a illustrates the HER polarization curves of these samples in N_2-saturated 1.0 M KOH

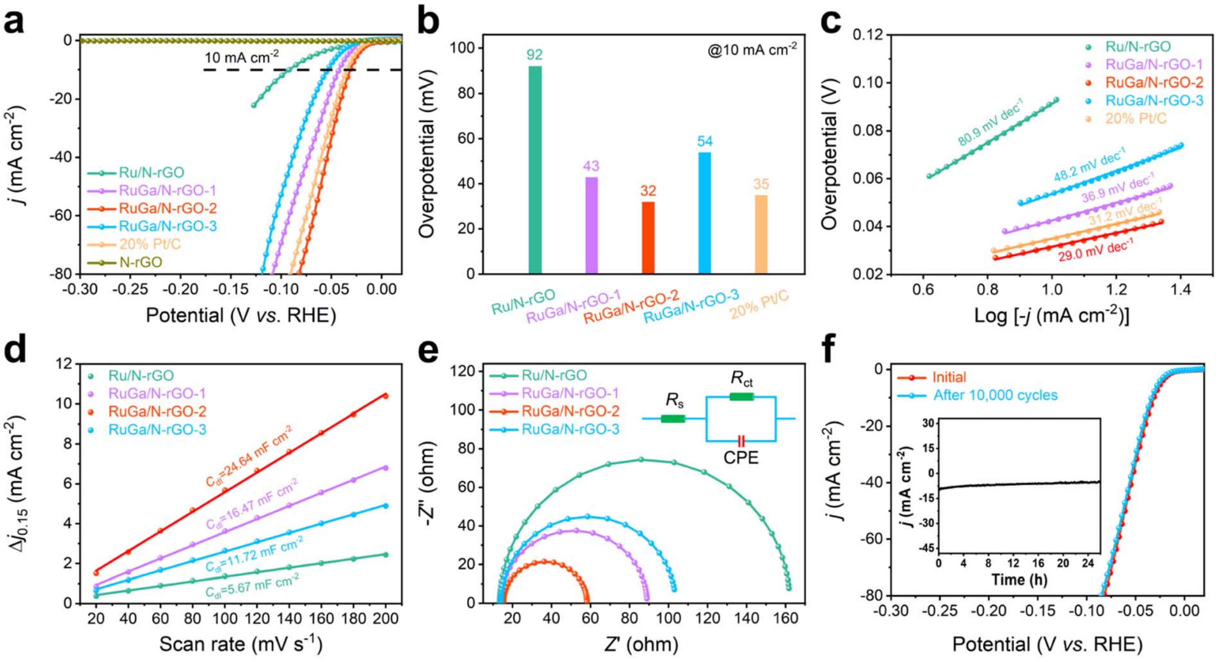

Fig. 3 (a) LSV curves of RuGa/N-rGO-*n* ($n = 1, 2, 3$), Ru/N-rGO, commercial Pt/C, and pure N-rGO towards acidic HER. (b) The histograms of overpotential values taken from the current density of 10 mA cm^{-2}. (c) The corresponding Tafel plots obtained from (a). (d) The calculated values of C_{dl}. (e) Nyquist plots measured at −0.03 V (inset: the related equivalent circuit for fitting the Nyquist plots). (f) LSV curves over RuGa/N-rGO-2 before and after the accelerated degradation tests (inset: chronoamperometric curve of RuGa/N-rGO-2 recorded at the constant overpotential of 30 mV for 26 hours).

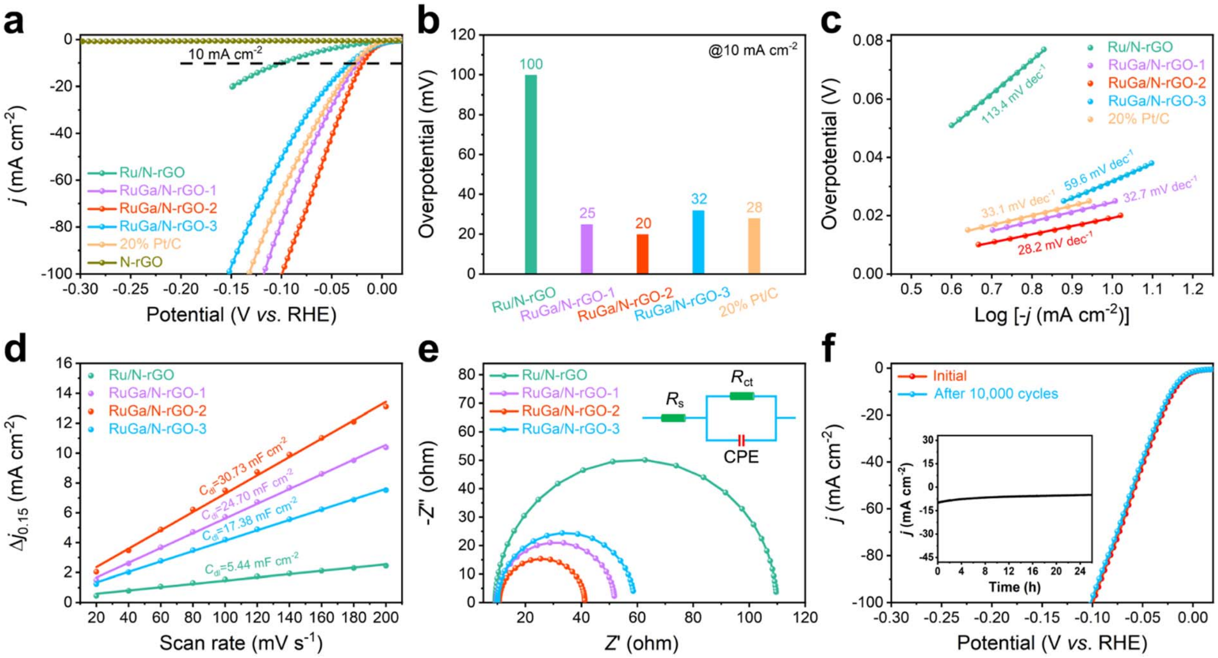

Fig. 4 (a) LSV curves of RuGa/N-rGO-*n* ($n = 1, 2, 3$), Ru/N-rGO, commercial Pt/C, and pure N-rGO towards alkaline HER. (b) The histograms of overpotential values taken from the current density of 10 mA cm^{-2}. (c) The corresponding Tafel plots obtained from (a). (d) The calculated values of C_{dl}. (e) Nyquist plots measured at −0.02 V (inset: the related equivalent circuit for fitting the Nyquist plots). (f) LSV curves over RuGa/N-rGO-2 before and after the accelerated degradation tests (inset: chronoamperometric curve of RuGa/N-rGO-2 recorded at the constant overpotential of 20 mV for 26 hours).

electrolyte. The value of overpotential for RuGa/N-rGO-2 is only 20 mV to reach 10 mA cm^{-2}, superior to those of RuGa/N-rGO-1 (25 mV), commercial Pt/C (28 mV), RuGa/N-rGO-3 (32 mV), and Ru/N-rGO (100 mV) (Fig. 4b). The calculated value of Tafel slope over RuGa/N-rGO-2 is 28.2 mV dec^{-1} (Fig. 4c), which is far lower than those of RuGa/N-rGO-1 (32.7 mV dec^{-1}), commercial Pt/C (33.1 mV dec^{-1}), RuGa/N-rGO-3 (59.6 mV dec^{-1}), and Ru/N-rGO (113.4 mV dec^{-1}), which indicates the favourable alkaline HER kinetics. The RuGa/N-rGO-2 is one of the best electrocatalysts for alkaline HER among the reported Ru-based electrocatalysts (Table S3†). In addition, RuGa/N-rGO-2 presents a higher C_{dl} value (Fig. 4d and S15†) and a smaller R_{ct} value (Fig. 4e). After 10 000 cycles, the LSV curves over RuGa/N-rGO-2 show a negligible shift (Fig. 4f). Moreover, the chronoamperometric curve could maintain a stable current density without degradation for 26 hours at the constant overpotential of 20 mV (inset of Fig. 4f), highlighting the outstanding electrochemical stability in alkaline electrolyte.

Large-scale industrial catalysis requires electrocatalysts with excellent activity and stability at large current densities. The large-current-density HER performances of RuGa/N-rGO-2 are measured in 1.0 M KOH electrolyte, in which the electrocatalyst is dropped directly onto the nickel foam (NF) with Ru amount of 0.5 mg cm^{-2}. The LSV polarization curves (Fig. 5a) reveal that RuGa/N-rGO-2 possesses extremely small overpotential values of 105 mV (500 mA cm^{-2}) and 156 mV (1000 mA cm^{-2}). Moreover, the Faraday efficiency is approximately 100% through measuring the amount of produced H_2 (Fig. 5b). The long-term durability at high current densities is also evaluated. As plotted in Fig. 5c, there is negligible shift in LSV polarization curves before and after 10 000 cycles. The long-term durability test proves that RuGa/N-rGO-2 can maintain its catalytic activity at the high current density of 500 mA cm^{-2} over 100 hours (Fig. 5d). Meanwhile, a series of structural characterizations of RuGa/N-rGO-2 after the long-term durability test reveal that the particle size, crystal structure, and morphology could be well-maintained (Fig. S16 and S17†), confirming its excellent structural stability. Impressively, the HER activities of RuGa/N-rGO-2 at high current densities are better than most representative electrocatalysts under alkaline environment (Fig. 5e and Table S4†). The excellent catalytic activity and stability of *bcc* RuGa can be attributed to its unique crystal structure. Specifically, (1) alloying Ru with Ga featuring lower electronegativity to form a structurally ordered intermetallic phase can cultivate electron-rich environments for the body-centered Ru atoms, thereby modulating the electronic structure of Ru sites and enhancing the catalytic performance. (2) The higher mixing enthalpy and stronger interactions between Ru and Ga atoms can strongly stabilize Ru atoms under harsh working conditions, which guarantees the robust stability. (3) Inserting Ga atoms into adjacent Ru atoms to obtain isolated Ru sites can maximize the utilization efficiency of noble metal atoms and expose active sites in a large proportion.

Density functional theory (DFT) calculations are adopted to elucidate the mechanism of improved performance in RuGa/N-rGO towards acidic and alkaline HER. Based on the previously reported theoretical results, the most stable RuGa (110) and Ru (001) facets are selected to establish reasonable theoretical models because of their lowest surface energies.[45,46] The 2D deformation charge density maps of Ru (001) and RuGa (110)

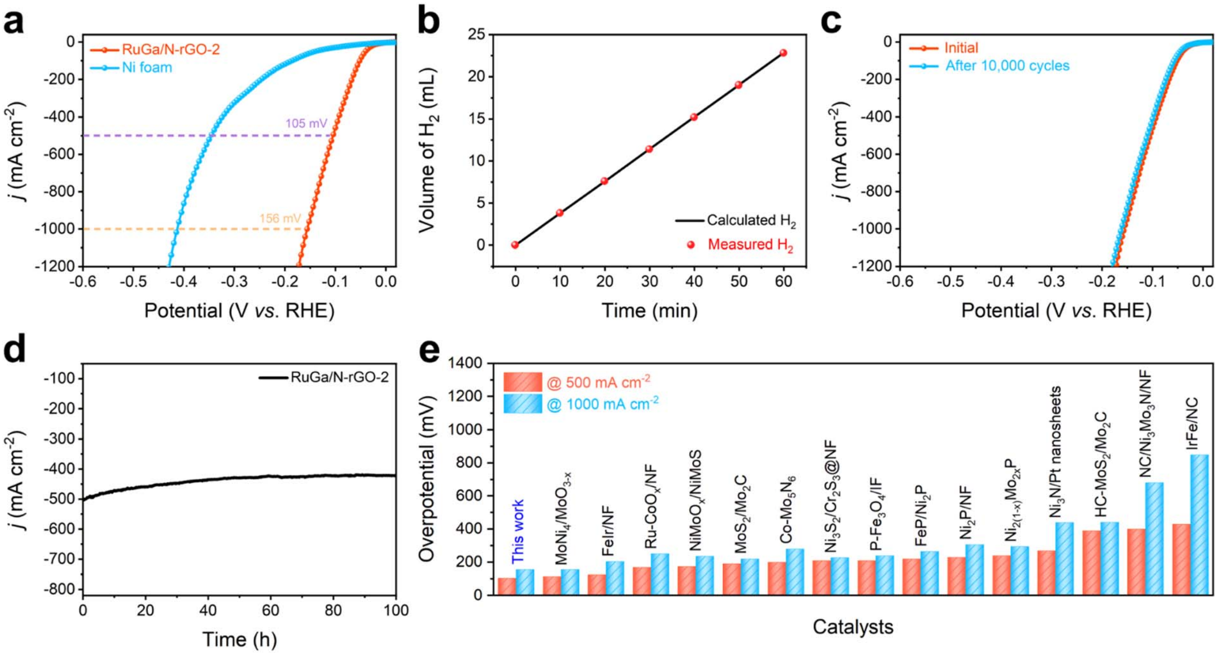

Fig. 5 (a) LSV curves of RuGa/N-rGO-2 and pure Ni foam for large-current-density HER in 1.0 M KOH electrolyte. (b) Theoretically calculated and experimentally measured H_2 gas amounts *versus* time over RuGa/N-rGO-2. (c) LSV curves for RuGa/N-rGO-2 before and after the accelerated degradation tests. (d) Chronoamperometric curve of RuGa/N-rGO-2 at the constant overpotential of 100 mV for 100 hours. (e) The comparison of overpotential values obtained at 500 and 1000 mA cm^{-2} between RuGa/N-rGO-2 and some reported electrocatalysts.

reveal that electrons from Ga atoms transfer to Ru atoms (Fig. 6a and b), which matches the results obtained from XPS analysis. The electrocatalysts with near-zero hydrogen adsorption free energy (ΔG_{*H}) usually exhibit remarkable HER performance.[47,48] The RuGa (110) shows a more optimal ΔG_{*H} value (−0.17 eV), which is much smaller relative to those of Pt (111) (−0.24 eV) and Ru (001) (−0.49 eV) (Fig. S18 and S19†), demonstrating a more favourable acidic HER performance of RuGa (110). The alkaline HER process involves three elementary steps, which begin with the Volmer step ($H_2O + e^- \rightarrow {*H} + OH^-$), subsequently occurring either the Heyrovsky step ($H_2O + {*H} + e^- \rightarrow H_2 + OH^-$) or Tafel step ($*H + {*H} \rightarrow H_2$).[49,50] Because of the relatively high energy barrier of water dissociation, the sluggish Volmer step is the rate-limiting step in the alkaline HER process.[51,52] The process of alkaline HER and the corresponding structural models are presented in Fig. 6c–e. The calculated value of water dissociation free energy barrier (ΔG_B) for RuGa (110) (0.48 eV) is smaller than those of Pt (111) (0.94 eV) and Ru (001) (0.75 eV) (Fig. S20–S22†). Moreover, RuGa (110) presents a relatively low value of ΔG_{*H} (−0.19 eV), which is

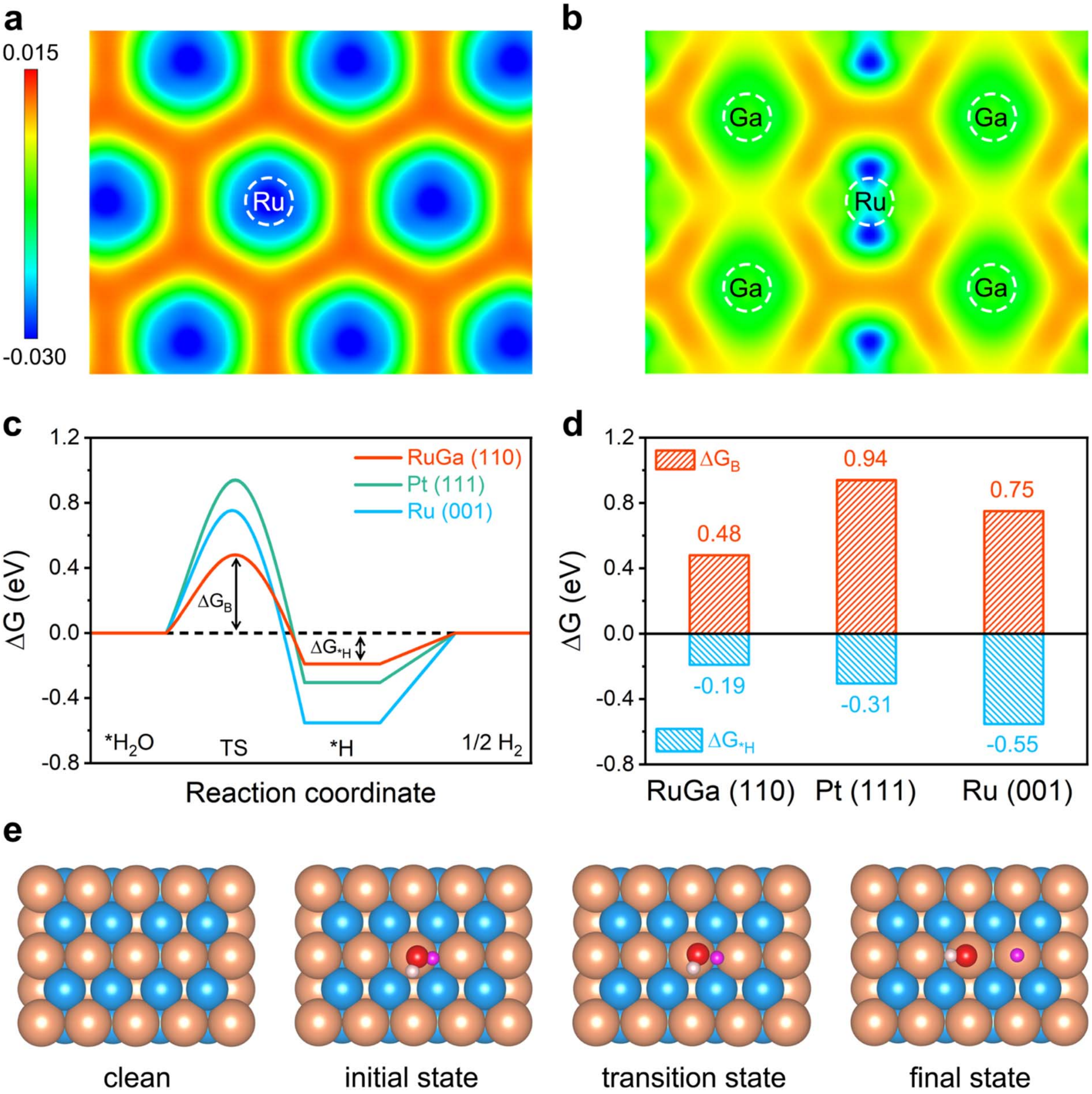

Fig. 6 Two-dimensional deformation charge density maps of (a) Ru (001) and (b) RuGa (110). The red area reflects the charge accumulation and the blue area indicates the charge depletion. (c) Gibbs free energy diagrams for alkaline HER over RuGa (110), Pt (111), and Ru (001). ΔG_B represents the water dissociation free energy barrier, and ΔG_{*H} refers to the hydrogen adsorption free energy. (d) The relationship between calculated ΔG_{*H} and ΔG_B values on RuGa (110), Pt (111), and Ru (001). (e) Structural models of water dissociation step on RuGa (110). Color codes: orange and blue spheres stand for Ru and Ga atoms. The red and white spheres correspond to the O and H atoms in an individual water molecule. Purple spheres represent the dissociated H atom adsorbed on RuGa (110).

much smaller compared with those of Pt (111) (−0.31 eV) and Ru (001) (−0.55 eV) (Fig. 6d). The above theoretical calculations demonstrate that the RuGa/N-rGO possesses the optimal HER performance in both acidic and alkaline electrolytes, which is consistent with the experimental results.

Conclusion

In summary, the RuGa/N-rGO materials are fabricated by a modified impregnation-reduction method. The extremely low overpotential values of synthesized catalysts are measured as 32 mV (acidic HER) and 20 mV (alkaline HER) at 10 mA cm^{-2}. In addition, the electrocatalyst requires only 105 mV and 156 mV to deliver 500 and 1000 mA cm^{-2} under alkaline medium, respectively, together with excellent durability (continuously operating at the overpotential of 100 mV for more than 100 hours). A series of structure characterizations and DFT calculations systematically illustrate that the Ru atoms with electron-rich environments are monodispersed in RuGa/N-rGO, which effectively reduces the energy barriers of the rate-limiting step towards the acidic and alkaline HER processes. This research could open up a new avenue for the rational design of noble metal-based nanomaterials for industrial hydrogen production.

Conflicts of interest

There are no conflicts to declare.

Acknowledgements

Q. L. acknowledges financial support from the National Natural Science Foundation of China (No. 92061119), the Beijing NOVA program (No. Z201100006820066 and 20220484172), the Fundamental Research Funds for the Central Universities (No. GJRC003), and the Guangdong Basic and Applied Basic Research Foundation (No. 2022A1515140051). A.-L. W. acknowledges financial support from the National Natural Science Foundation of China (No. 22005176) and the Natural Science Foundation of Shandong Province (No. ZR2020QE014).

Notes and references

1 L. Li, L. Bu, B. Huang, P. Wang, C. Shen, S. Bai, T.-S. Chan, Q. Shao, Z. Hu and X. Huang, *Adv. Mater.*, 2021, **33**, 2105308.

2 Q. Yu, X. Liu, G. Liu, X. Wang, Z. Li, B. Li, Z. Wu and L. Wang, *Adv. Funct. Mater.*, 2022, **32**, 2205767.

3 G. Fu, X. Kang, Y. Zhang, X. Yang, L. Wang, X.-Z. Fu, J. Zhang, J.-L. Luo and J. Liu, *Nano-Micro Lett.*, 2022, **14**, 200.

4 Q. Liang, Q. Li, L. Xie, H. Zeng, S. Zhou, Y. Huang, M. Yan, X. Zhang, T. Liu, J. Zeng, K. Liang, O. Terasaki, D. Zhao, L. Jiang and B. Kong, *ACS Nano*, 2022, **16**, 7993–8004.

5 Z. Liu, L. Zeng, J. Yu, L. Yang, J. Zhang, X. Zhang, F. Han, L. Zhao, X. Li, H. Liu and W. Zhou, *Nano Energy*, 2021, **85**, 105940.

6 Y.-L. Wu, X. Li, Y.-S. Wei, Z. Fu, W. Wei, X.-T. Wu, Q.-L. Zhu and Q. Xu, *Adv. Mater.*, 2021, **33**, 2006965.

7 Z. Jiang, S. Song, X. Zheng, X. Liang, Z. Li, H. Gu, Z. Li, Y. Wang, S. Liu, W. Chen, D. Wang and Y. Li, *J. Am. Chem. Soc.*, 2022, **144**, 19619–19626.

8 X. Chen, J. Wan, J. Wang, Q. Zhang, L. Gu, L. Zheng, N. Wang and R. Yu, *Adv. Mater.*, 2021, **33**, 2104764.

9 J. Wang, S. Xin, Y. Xiao, Z. Zhang, Z. Li, W. Zhang, C. Li, R. Bao, J. Peng, J. Yi and S. Chou, *Angew. Chem., Int. Ed.*, 2022, **61**, e202202518.

10 H. Liu, R. Xie, Y. Luo, Z. Cui, Q. Yu, Z. Gao, Z. Zhang, F. Yang, X. Kang, S. Ge, S. Li, X. Gao, G. Chai, L. Liu and B. Liu, *Nat. Commun.*, 2022, **13**, 6382.

11 L. A. King, M. A. Hubert, C. Capuano, J. Manco, N. Danilovic, E. Valle, T. R. Hellstern, K. Ayers and T. F. Jaramillo, *Nat. Nanotechnol.*, 2019, **14**, 1071–1074.

12 V. R. Jothi, K. Karuppasamy, T. Maiyalagan, H. Rajan, C.-Y. Jung and S. C. Yi, *Adv. Energy Mater.*, 2020, **10**, 1904020.

13 J. Mao, C.-T. He, J. Pei, W. Chen, D. He, Y. He, Z. Zhuang, C. Chen, Q. Peng, D. Wang and Y. Li, *Nat. Commun.*, 2018, **9**, 4958.

14 S. Shen, Z. Hu, H. Zhang, K. Song, Z. Wang, Z. Lin, Q. Zhang, L. Gu and W. Zhong, *Angew. Chem., Int. Ed.*, 2022, **61**, e202206460.

15 J. Zhang, Y. Zhao, X. Guo, C. Chen, C.-L. Dong, R.-S. Liu, C.-P. Han, Y. Li, Y. Gogotsi and G. Wang, *Nat. Catal.*, 2018, **1**, 985–992.

16 Q. Yu, Z. Zhang, S. Qiu, Y. Luo, Z. Liu, F. Yang, H. Liu, S. Ge, X. Zou, B. Ding, W. Ren, H.-M. Cheng, C. Sun and B. Liu, *Nat. Commun.*, 2021, **12**, 6051.

17 X. Mu, X. Gu, S. Dai, J. Chen, Y. Cui, Q. Chen, M. Yu, C. Chen, S. Liu and S. Mu, *Energy Environ. Sci.*, 2022, **15**, 4048–4057.

18 J. Li, Y. Li, J. Wang, C. Zhang, H. Ma, C. Zhu, D. Fan, Z. Guo, M. Xu, Y. Wang and H. Ma, *Adv. Funct. Mater.*, 2022, **32**, 2109439.

19 X. Wu, Z. Wang, D. Zhang, Y. Qin, M. Wang, Y. Han, T. Zhan, B. Yang, S. Li, J. Lai and L. Wang, *Nat. Commun.*, 2021, **12**, 4018.

20 Q. Li, F. Huang, S. Li, H. Zhang and X.-Y. Yu, *Small*, 2022, **18**, 2104323.

21 C. Cai, K. Liu, Y. Zhu, P. Li, Q. Wang, B. Liu, S. Chen, H. Li, L. Zhu, H. Li, J. Fu, Y. Chen, E. Pensa, J. Hu, Y. R. Lu, T. S. Chan, E. Cortes and M. Liu, *Angew. Chem., Int. Ed.*, 2022, **61**, e202113664.

22 H. Zhang, Y. Li, C. Cheng, J. Zhou, P. Yin, H. Wu, Z. Liang, J. Zhang, Q. Yun, A.-L. Wang, L. Zhu, B. Zhang, W. Cao, X. Meng, J. Xia, Y. Yu and Q. Lu, *Angew. Chem., Int. Ed.*, 2023, **62**, e202213351.

23 W.-J. Zeng, C. Wang, Q.-Q. Yan, P. Yin, L. Tong and H.-W. Liang, *Nat. Commun.*, 2022, **13**, 7654.

24 T.-W. Song, C. Xu, Z.-T. Sheng, H.-K. Yan, L. Tong, J. Liu, W.-J. Zeng, L.-J. Zuo, P. Yin, M. Zuo, S.-Q. Chu, P. Chen and H.-W. Liang, *Nat. Commun.*, 2022, **13**, 6521.

25 C.-L. Yang, L.-N. Wang, P. Yin, J. Liu, M.-X. Chen, Q.-Q. Yan, Z.-S. Wang, S.-L. Xu, S.-Q. Chu, C. Cui, H. Ju, J. Zhu, Y. Lin, J. Shui and H.-W. Liang, *Science*, 2021, **374**, 459–464.

26 Y. Niu, Y. Wang, J. Chen, S. Li, X. Huang, M.-G. Willinger, W. Zhang, Y. Liu and B. Zhang, *Sci. Adv.*, 2022, **8**, eabq5751.

27 H. Zhang, P. Shi, X. Ma, C. Ma, S. Han, C. He, H. Wu, L. Zhu, B. Zhang, Y. Lu, W. Cao, H. Yin, X. Meng, J. Xia, J. Zhang, A.-L. Wang and Q. Lu, *Adv. Energy Mater.*, 2023, **13**, 2202703.

28 Z. Lin, B. Xiao, M. Huang, L. Yan, Z. Wang, Y. Huang, S. Shen, Q. Zhang, L. Gu and W. Zhong, *Adv. Energy Mater.*, 2022, **12**, 2200855.

29 D. Chen, Z. Pu, P. Wang, R. Lu, W. Zeng, D. Wu, Y. Yao, J. Zhu, J. Yu, P. Ji and S. Mu, *ACS Catal.*, 2022, **12**, 2623–2631.

30 Z. Zhang, J. Tian, Y. Lu, X. Gou, J. Li, W. Hu, W. Lin, R. S. Kim and J. Fu, *Angew. Chem., Int. Ed.*, 2022, **61**, e202202017.

31 T. Zhao, G. Wang, M. Gong, D. Xiao, Y. Chen, T. Shen, Y. Lu, J. Zhang, H. Xin, Q. Li and D. Wang, *ACS Catal.*, 2020, **10**, 15207–15216.

32 J. Liang, F. Ma, S. Hwang, X. Wang, J. Sokolowski, Q. Li, G. Wu and D. Su, *Joule*, 2019, **3**, 956–991.

33 M. Luo, Y. Sun, L. Wang and S. Guo, *Adv. Energy Mater.*, 2017, **7**, 1602073.

34 G. Fu, X. Yan, Y. Chen, L. Xu, D. Sun, J.-M. Lee and Y. Tang, *Adv. Mater.*, 2018, **30**, 1704609.

35 M. Li, Y. Wang, Y. Zheng, G. Fu, D. Sun, Y. Li, Y. Tang and T. Ma, *Adv. Energy Mater.*, 2020, **10**, 1903833.

36 X. Tian, X. Zhao, Y.-Q. Su, L. Wang, H. Wang, D. Dang, B. Chi, H. Liu, E. J. M. Hensen, X. W. Lou and B. Y. Xia, *Science*, 2019, **366**, 850–856.

37 L. Gao, X. Li, Z. Yao, H. Bai, Y. Lu, C. Ma, S. Lu, Z. Peng, J. Yang, A. Pan and H. Huang, *J. Am. Chem. Soc.*, 2019, **141**, 18083–18090.

38 Y. Li, X. F. Lu, S. Xi, D. Luan, X. Wang and X. W. Lou, *Angew. Chem., Int. Ed.*, 2022, **61**, e202201491.

39 G. Zhu, Y. Jiang, H. Yang, H. Wang, Y. Fang, L. Wang, M. Xie, P. Qiu and W. Luo, *Adv. Mater.*, 2022, **34**, 2110128.

40 S. Han, C. He, Q. Yun, M. Li, W. Chen, W. Cao and Q. Lu, *Coord. Chem. Rev.*, 2021, **445**, 214085.

41 Y. Yan, J. S. Du, K. D. Gilroy, D. Yang, Y. Xia and H. Zhang, *Adv. Mater.*, 2017, **29**, 1605997.

42 L. Bai, X. Wang, Q. Chen, Y. Ye, H. Zheng, J. Guo, Y. Yin and C. Gao, *Angew. Chem., Int. Ed.*, 2016, **55**, 15656–15661.

43 D. Wang, H. L. Xin, R. Hovden, H. Wang, Y. Yu, D. A. Muller, F. J. DiSalvo and H. D. Abruña, *Nat. Mater.*, 2013, **12**, 81–87.

44 Q. Hu, K. Gao, X. Wang, H. Zheng, J. Cao, L. Mi, Q. Huo, H. Yang, J. Liu and C. He, *Nat. Commun.*, 2022, **13**, 3958.

45 K. D. Gilroy, A. Ruditskiy, H.-C. Peng, D. Qin and Y. Xia, *Chem. Rev.*, 2016, **116**, 10414–10472.

46 H. Chen, X. Ai, W. Liu, Z. Xie, W. Feng, W. Chen and X. Zou, *Angew. Chem., Int. Ed.*, 2019, **58**, 11409–11413.

47 F. Bao, Z. Yang, Y. Yuan, P. Yu, G. Zeng, Y. Cheng, Y. Lu, J. Zhang and H. Huang, *Adv. Funct. Mater.*, 2022, **32**, 2108991.

48 J. Zhang, Q. Zhang and X. Feng, *Adv. Mater.*, 2019, **31**, 1808167.

49 J. Wei, M. Zhou, A. Long, Y. Xue, H. Liao, C. Wei and Z. J. Xu, *Nano-Micro Lett.*, 2018, **10**, 75.

50 R. Subbaraman, D. Tripkovic, D. Strmcnik, K.-C. Chang, M. Uchimura, A. P. Paulikas, V. Stamenkovic and N. M. Markovic, *Science*, 2011, **334**, 1256–1260.

51 K. Xu, H. Cheng, H. Lv, J. Wang, L. Liu, S. Liu, X. Wu, W. Chu, C. Wu and Y. Xie, *Adv. Mater.*, 2018, **30**, 1703322.

52 F. Hu, D. Yu, M. Ye, H. Wang, Y. Hao, L. Wang, L. Li, X. Han and S. Peng, *Adv. Energy Mater.*, 2022, **12**, 2200067.